
HIGH PERFORMANCE SPACE DEBRIS TRACKING IN COMPLEX SKYLIGHT BACKGROUNDS WITH A LARGE-SCALE DATASET

Guohang Zhuang^{1,2*}, Weixi Song^{3*}, Jinyang Huang¹, Chenwei Yang⁴, Wanli Ouyang^{2,5}, Yan Lu^{2,5†}

¹Hefei University of Technology, ²Shanghai Artificial Intelligence Laboratory,

³Zhejiang University, ⁴Polar Research Institute of China,

⁵The Chinese University of Hong Kong

July 28, 2025

ABSTRACT

With the rapid development of space exploration, space debris has attracted more attention due to its potential extreme threat, leading to the need for real-time and accurate debris tracking. However, existing methods are mainly based on traditional signal processing, which cannot effectively process the complex background and dense space debris. In this paper, we propose a deep learning-based Space Debris Tracking Network (SDT-Net) to achieve highly accurate debris tracking. SDT-Net effectively represents the feature of debris, enhancing the efficiency and stability of end-to-end model learning. To train and evaluate this model effectively, we also produce a large-scale dataset Space Debris Tracking Dataset (SDTD) by a novel observation-based data simulation scheme. SDTD contains 18,040 video sequences with a total of 62,562 frames and covers 250,000 synthetic space debris. Extensive experiments validate the effectiveness of our model and the challenging of our dataset. Furthermore, we test our model on real data from the Antarctic Station, achieving a MOTA score of 73.2%, which demonstrates its strong transferability to real-world scenarios. Our dataset and code will be released soon.

1 Introduction

During the past decade, global space activities have exponentially increased, which has raised the potential risk of collisions between debris and spacecraft in near-Earth space [1, 2]. This has led to significant economic losses, drawing increasing attention to the issue of space debris. The Space Debris Tracking (SDT) is to detect and predict the trajectories of space debris, reducing the collision risks and promoting space industry development. This makes monitoring debris extremely urgent and critical for ensuring the safety of space operations.

SDT is an essential task that includes detecting and predicting the trajectories of space debris. It is a computer vision problem, specifically an object tracking task in astronomical videos, where the goal is to identify and follow space debris across continuous frames for a video. However, traditional methods typically focus on object debris detection rather than tracking. These approaches often rely on techniques such as template-matching methods [3, 4] and morphological operator methods [5, 6]. While these methods are capable of detecting debris in individual images, they struggle to associate objects across consecutive frames, making them less suitable for space debris monitoring.

Artificial intelligence (AI) has achieved significant success in fields such as object detection [7] and object tracking [8], due to its exceptional ability to process large-scale datasets. Traditional methods have limitations in space debris detection and cannot effectively handle long-term tracking tasks. AI models can make up for this deficiency through efficient data processing and learning methods. However, AI models rely on large-scale, high-quality datasets while astronomy data are extremely limited. So, there is no an effective AI model that could meet the requirements

*Equal contribution.

†Corresponding author.

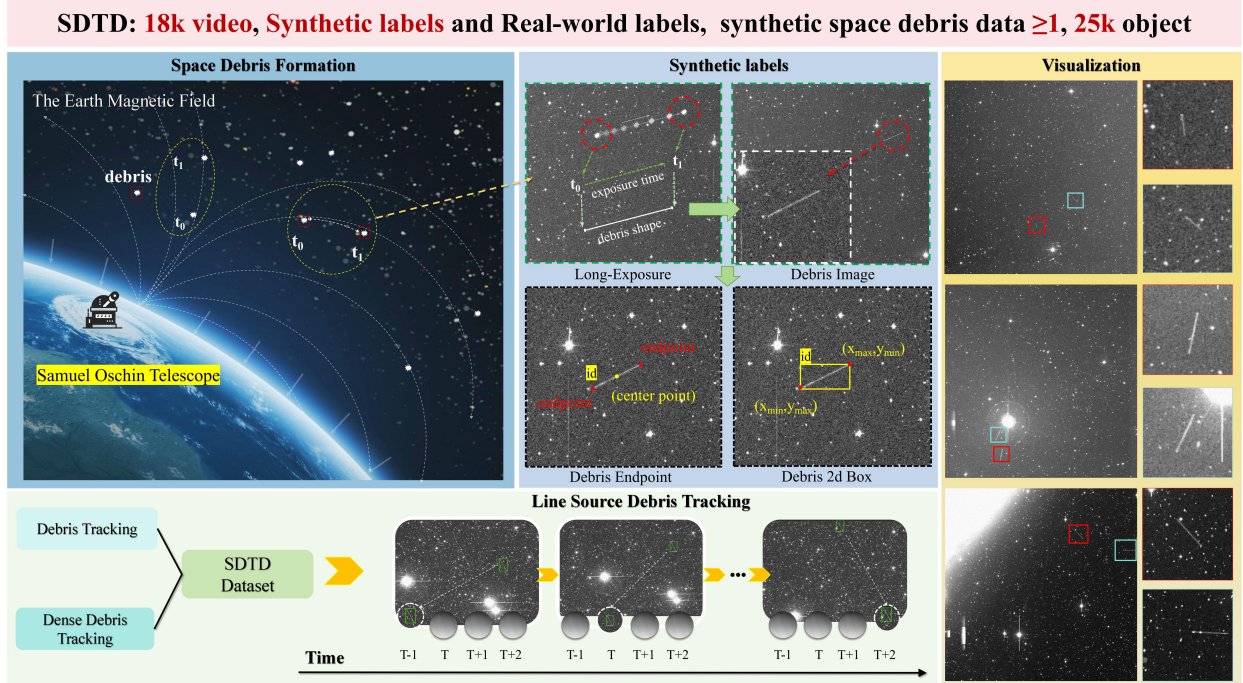


Figure 1: Illustration of the space debris formation and tracking pipeline using synthetic labels. It includes the simulation of space debris within Earth’s magnetic field, the generation of synthetic labels such as start (st), end (ed), and center (cen) points, and bounding boxes for debris in image frames. Additionally, the process of segment source debris tracking across multiple frames is shown, with visualization examples of debris tracking and dense debris tracking using the SDTD dataset.

of debris tracking mission for popular telescopes like the Solar Data Telescope (LST) [9] and Wide-Field Survey Telescope (WFST) [10].

To address the challenge of limited data in astronomy, we follow the idea of observation-based data simulation in the astronomical field [11, 12, 13]. The observation-based data simulation is widely proven to lead to realistic data and reliable scientific conclusions, providing a chance for us to design a method for data simulating space debris. Due to its success, we construct a Space Debris Tracking Dataset (SDTD), which is the first publicly available dataset designed for space debris tracking. Fig 1 shows the formation principle, type, examples, and corresponding SDT tasks of space debris. Specifically, Tab 1 highlights the key differences of SDTD compared to existing datasets. SDTD consists of 18,040 synthetic videos, totaling 62,562 frames and 25,000 annotated debris instances.

In order to apply AI methods to the SDT task, we propose a simple yet effective deep learning method, namely the Space Debris Tracking Network (SDT-Net). We introduce a Region-of-Interest Feature Enhancement (RoIFE) module to highlight debris features, aiding in more accurate detection. A detection module is then used to localize the debris by predicting their positions in the image. After localization, a debris offset module is applied to perform cross-frame data association, generating tracking trajectories for each debris.

In summary, the key contributions of this paper are as follows:

1. We propose a space debris simulation method. Based on this method, we construct SDTD, the first benchmark dataset for SDT. It contains 18,040 video data with complex backgrounds and diverse debris targets, and the data is close to the real space debris situation.
2. We introduce the Space Debris Tracking Network (SDT-Net) to improve space debris tracking. By integrating a RoIFE module, a detection module, and a tracking module, we effectively enhance debris representations, leading to more accurate and reliable tracking performance.
3. Evaluation on the constructed SDTD dataset shows that the proposed SDT-Net achieves state-of-the-art performance in terms of space debris tracking on the test set overall.

Table 1: Summary of Space Debris Target Datasets.

Dataset	Type	Size	#Video.	#Det.	#Seg.	#Track.	Target Variations	Debris Number
Lin et al. [11]	Real	83 images	7 video	✓	×	×	One	One
SDebrisNet [14]	Real	1551 images	×	✓	×	×	Three	One
Jiang et al. [6]	Real	200 images	×	✓	×	×	One	One
AstroStripeSet [15]	Real	1500 images	×	✓	✓	×	Four	One
SDTD	Synthetic & Real	65,562 images	18,040 video	✓	✓	✓	Five	One to Five

2 Related Work

2.1 Object Detection and Tracking

Object detection and tracking involves detecting objects, assigning a unique ID to each detection, and then tracking these objects across frames in a video while maintaining the ID assignments. This task has been a central focus in computer vision and has found applications in various fields, such as autonomous driving [16].

In the context of tracking, several methods have been proposed over the years. For instance, SORT [17] conducted track association by combining Kalman Filter [18] and Hungarian algorithm [19]. DeepSORT [20] introduced an extra cosine distance and compute the appearance similarity for track association. CenterTrack [21] is a center-based multi-object tracking method that extends the detection framework of CenterNet [22] to achieve efficient real-time tracking. ByteTrack [23] exploits low-score detection boxes by first matching high-confidence detections and then associating them with low-score detections.

2.2 Space Debris Detection

Space Debris Detection is a task of predicting space debris location from a single image. Jiang et al. [24] applied enhanced median filtering to remove noise and used an improved Hough transform to detect targets. Guo et al. [25] proposed an enhanced YOLOv8-based method for space debris detection, achieving improved accuracy and speed. Jia et al. [26] proposed a deep neural network-based framework for detecting and classifying astronomical targets. Specifically, they utilized Faster R-CNN [27] with a modified ResNet-50 [28] backbone to improve the detection of low signal-to-noise targets. Previous studies have primarily focused on detection tasks, limiting their applications in space debris. In this paper, we extend the detection to tracking, playing a key role in advancing space exploration.

3 Benchmark Dataset

In this paper, we utilize astronomical images collected by the Zwicky Transient Facility (ZTF) [29] to simulate space debris. We propose a simulation tool to generate space debris, which provides sufficient data for constructing the SDTD dataset. Under long-exposure conditions in telescopic observations, debris often appears as a line source in the images. So, our simulation target is to generate realistic long-exposure line sources. We develop a pipeline that includes data pre-processing, line source debris video generation, and post processing. Fig 2 and the following paragraphs provide a detailed description of this process.

3.1 Data Collection and Pre-Processing

3.1.1 Data Collection

The ZTF is an optical survey project designed to monitor astronomical transient phenomena. It operates on the 48-inch Samuel Oschin Telescope at Palomar Observatory, using a 47-square-degree, 600-megapixel CCD camera for high-cadence, wide-field imaging. Its capability to capture large-scale, high-resolution astronomical images makes it suitable for simulating space debris.

In order to obtain enough data for simulation, we collected 17,235 ZTF astronomical observation data from June 2018 to June 2022. These data contain complex skylight background information, including atmospheric scattered light, moonlight, and human factors such as light pollution. Based on these richer astronomical observation data, we conduct simulations and generated debris videos.

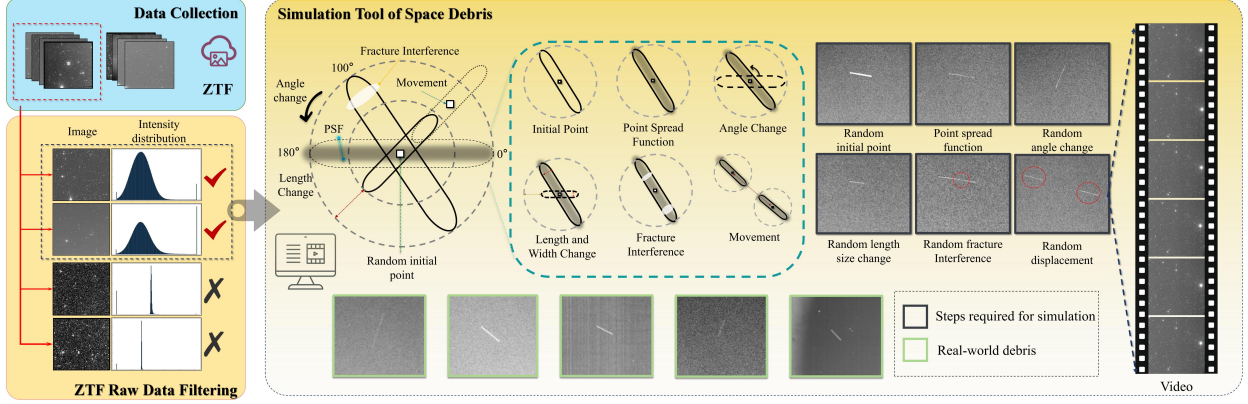


Figure 2: Overview of the space debris simulation pipeline. Step 1: Data Collection. Step 2: ZTF Raw Data Filtering. Step 3: Simulation Tool for Space Debris. Various parameters, including random initial points, angle change, length change, point spread function (PSF), fracture interference, and displacement, are applied to simulate space debris. The process generates synthetic video sequences and shows the real-world debris for reference.

Some regions of the images contain outliers, appearing as zeros or extremely high values, which leads to numerical overflow issues. To ensure the quality of our dataset, we carefully examine the dataset, remove 1,195 unusable images, and retain 16,040 high-quality images.

3.1.2 Data Pre-Processing

Unlike natural images, astronomical images typically contain larger pixel values. Therefore, a data processing step is necessary to transform these values into the standard range of grayscale image pixels. To achieve this, we apply the ZScale method [30] to map image pixel values to a reasonable range. The ZScale method first calculates the median z_{median} and standard deviation z_{std} of the image pixels. Then uses these two values to estimate a range $[z_1, z_2]$:

$$z_1 = z_{median} - k \times z_{std}, z_2 = z_{median} + k \times z_{std}, \quad (1)$$

where z_1 and z_2 represent the lower and upper bounds of the pixel intensity range, respectively. The hyperparameter k is assigned a value of 2.5. Then, we perform a linear stretch on the grayscale values of the image, mapping the range $[z_1, z_2]$ to $[0, 255]$:

$$I_{scaled}(x, y) = 255 \times \frac{I(x, y) - z_1}{z_2 - z_1}. \quad (2)$$

Finally, pixels with grayscale values below z_1 or above z_2 are set to 0 or 255:

$$I_{final}(x, y) = \begin{cases} \max(I_{scale}(x, y), 0), & I_{scale}(x, y) < 0 \\ \min(I_{scale}(x, y), 255), & I_{scale}(x, y) > 0 \end{cases} \quad (3)$$

By enhancing the contrast and detail of astronomical images, the ZScale method ensures a reliable basis for the next simulations.

After pre-processing the data, we conduct simulations to generate space debris, providing sufficient data for constructing the SDTD dataset. Details of the simulation process are described in Section 3.2.

3.2 Simulation of Space Debris

For a single astronomical image, the Space Debris Simulation generates a video with T frames of line source debris, simulating the movement of debris across each frame.

3.2.1 Line Source Debris Video Generation

The goal of the space debris simulation is to generate a sequence video with multiple line source debris. For each debris (set k -th as an example), we represent it as a parameter sequence $\{S_k^1, S_k^2, S_k^3, \dots, S_k^T\}$ where T is the total frame number.

S_k^t is the debris parameters for the t -th frame, which is set as follows:

$$S_k^t = \underbrace{\{x_k^t, y_k^t\}}_{\text{center}}, \underbrace{\{l_k, w_k\}}_{\text{dimension}}, \underbrace{\{\theta_k, v_k\}}_{\text{velocity}}, \quad (4)$$

where (x_k^t, y_k^t) represents center point coordinates of the line source at time t . l_k, w_k, θ_k and v_k are line length, line width, velocity angle and velocity magnitude, respectively.

With this parametrized line source, we randomly sample a value K as the total line source number and then for the k -th line source, we first generate its S_k^1 by randomly sampling its 6 parameters. The generated S_k^1 provide the initial center point locations, defined dimension, and a fixed velocity of the debris. So, we utilize these parameters to produce subsequent parameters $S_k^2 \sim S_k^T$.

Take the second frame ($t = 2$) as an example, we calculate the parameters for S_k^2 . The center point coordinates (x_k^2, y_k^2) is calculated by combining velocity and initial center as follows:

$$\begin{aligned} x_k^2 &= x_k^1 + v_k \cdot \cos(\theta_k) \cdot \Delta t, \\ y_k^2 &= y_k^1 + v_k \cdot \sin(\theta_k) \cdot \Delta t, \end{aligned} \quad (5)$$

where Δt represents the time interval between consecutive frames, which is set to 1 here for simplification. Thus, the parameters for the second frame are represented as $S_k^2 = \{x_k^2, y_k^2, l_k, w_k, \theta_k, v_k\}$. The same procedure is repeated for each subsequent frame $t = \{3, 4, 5, \dots, T\}$. This process continues frame by frame, until all parameters $\{S_k^1, S_k^2, S_k^3, \dots, S_k^T\}$ are generated.

We proceed to generate the corresponding line source in the image. For each frame t , we take the parameters $S_k^t = \{x_k^t, y_k^t, l_k, w_k, \theta_k, v_k\}$ and follow three steps to generate the line source. With these, at the center point coordinates (x_k^t, y_k^t) , we draw a rectangle with dimensions, l_k and w_k , and angle θ_k . Then, we apply random brightness noise to the rectangle. By traversing k , we draw entire K objects and if the rectangle is out of the image, we would neglect it.

At last, using the parameters $\{S_k^1, S_k^2, S_k^3, \dots, S_k^T\}$, we generate the corresponding images $\{I^1, I^2, I^3, \dots, I^T\}$, resulting in a video that captures the movement trajectory of the debris.

3.2.2 Post Processing for Realistic

Since the real line source debris conforms to the Point Spread Function (PSF) characteristics [31], we perform point diffusion function processing on the preliminary line source debris. Among them, PSF is expressed as follows:

$$I_k^t(x, y) = \frac{S}{2\pi\delta_{psf}^2} \exp\left(-\frac{(x - x_c)^2 + (y - y_c)^2}{2\delta_{psf}^2}\right), \quad (6)$$

where $I_k^t(x, y)$ is the pixel value of the line source debris, (x_c, y_c) represents the center point coordinates of the line source debris, S is the scale factor, and δ_{psf} is the diffusion standard deviation of the imaging system PSF. Additionally, we apply random truncation to the line source to simulate more realistic conditions. This operation enables us to simulate realistic line source debris.

3.3 Statistics and Visualization

3.3.1 Dataset Statistics

After the simulation, we obtain 18,040 videos with a total of 62,562 frames. As shown in Fig. 12(a), to evaluate model performance in complex environments, we select 1,000 images from the 16,040 dataset to create two test sets: the debris test set and the dense debris test set. These two test sets allow for a comprehensive evaluation of model robustness under different conditions, including dense debris.

3.3.2 Debris Type

To facilitate comprehensive evaluation of model performance at different levels of complexity, we classify the space debris in our dataset into two categories: debris type and dense debris type. This distinction allows us to systematically evaluate tracking robustness in both sparse and complex observation environments.

Debris type refers to space objects that appear singly or sparsely in an observation frame. These objects are separated from each other with limited spatial or temporal overlap, and are therefore relatively easy to detect and track. In contrast,

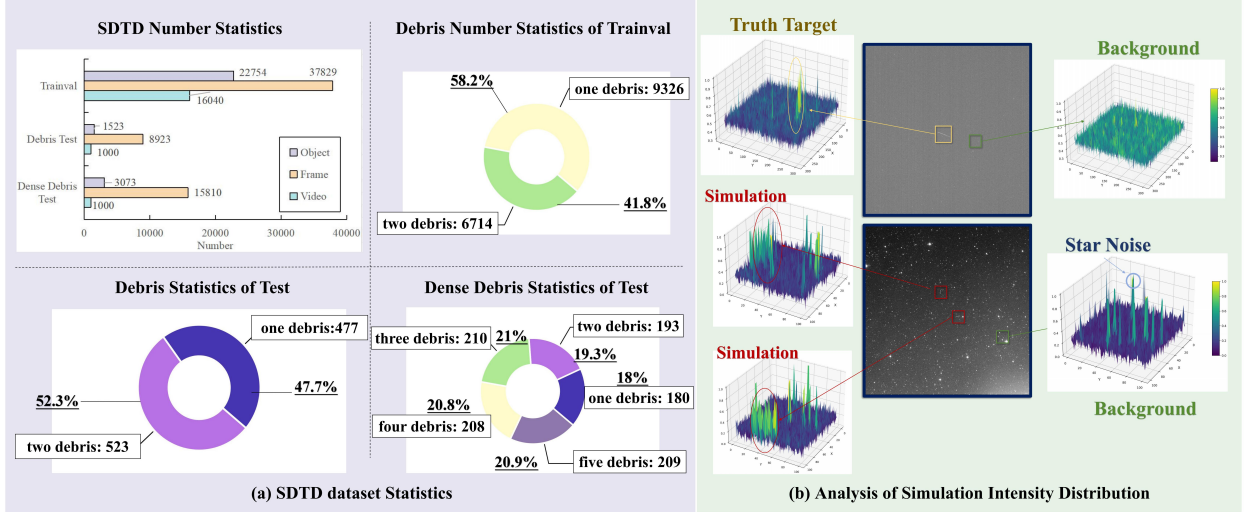


Figure 3: Overview of SDTD dataset statistics and analysis of debris simulation intensity distribution. (a) The left shows the number statistics for training, test, and dense debris categories in the SDTD dataset. The pie charts represent the distribution of debris across different objects in both the training and test sets. (b) The right displays the analysis of simulation intensity distribution, comparing the target, simulation, background, and star noise. It also shows the intensity distribution for debris and background noise.

dense debris type represents scenes with high target density, where multiple debris objects (usually more than three) appear within a single frame or between adjacent frames. These instances typically exhibit significant spatial overlap and motion correlation, which increases the difficulty of identity assignment and temporal association.

3.3.3 Simulation Visualization

Line source debris in the image generally exhibits high-intensity values. To better compare the effect of simulated line source debris, we visualize the intensity distribution of the image. Fig 12(b) shows the intensity distribution analysis of the target image. On the left side of the image, we visualized the intensity distribution of different regions in three dimensions. In the yellow box area, we show the intensity distribution of the real target, which shows obvious concentrated peaks, representing the intensity characteristics of the real celestial body. These peaks indicate the concentrated distribution area of the target signal.

In contrast, the red box area shows the target distribution generated by simulation, and the intensity distribution of the simulated target shows a similar trend. In addition, the green box area in the image shows the intensity distribution of the background noise. In the simulated image, the background noise (such as star noise) shows multiple peaks, indicating that the distribution of the noise is more dispersed, and strong interference signals appear in some areas. By comparing these distributions, we can verify the effectiveness of the simulation and confirm that the simulated data can still accurately retain the basic structural characteristics of the target under the influence of background noise.

4 Method

4.1 Overview

The entire pipeline of our Space Debris Tracking Network (SDT-Net) method is shown in Fig. 4, which is a CenterTrack-style [21] tracking method. Due to the debris long-exposure as linear, we treat the debris tracking as tracking for linear segments. For each object, we follow the tracking-by-detection idea. Our model detects two endpoints of each line and predicts velocity for cross-frame object association to generate trajectory.

Specifically, a backbone extract base features for each frame, we establish a Region-of-Interest Feature Enhancement (RoI-FE) module to highlight the debris object cues in feature maps. Then, a novel design detection module consists of an endpoint heatmap head and a line source embedding head that collaborate to localize two endpoints of each debris. After that, a tracking head predicts velocity for each object by computing endpoint offsets across frames.

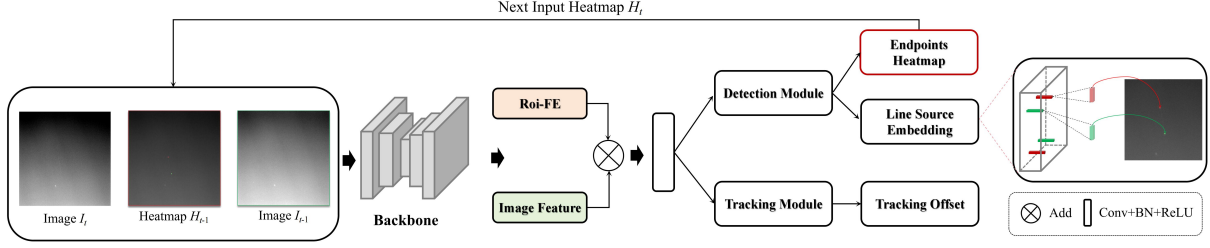


Figure 4: The overall pipeline of our SDT-Net. The inputs are the current frame I_t , the previous frame I_{t-1} and heatmap H_{t-1} . The outputs include amodal endpoints heatmap, line source embedding, and tracking offset.

4.2 Backbone

For the t -th frame, the model takes three components as inputs, the image of the current frame, the previous frame and its predicted endpoints representing as heatmaps. Each input is passed through a corresponding input-dependent module containing a convolutional layer, a batch normalization layer, and a ReLU activation function. After this, the three feature maps are added together, resulting in a unified feature map $F_{input} \in \mathcal{R}^{W_{in} \times H_{in} \times 3}$. The feature map F_{input} is then passed through our backbone, a DLA model [32], which consists of an encoder and a decoder. The encoder outputs a series of feature maps at different resolutions, denoted as $\{F_1, F_2, F_3, F_4\}$. The decoder, an IDA up-sampler [32], takes these feature maps to gradually generate upsampled feature maps and we take the highest resolution one as our backbone feature $F_b \in \mathcal{R}^{W \times H \times C}$.

4.3 Region-of-Interest Feature Enhancement

The Region-of-Interest Feature Enhancement module first computes a debris mask. Specifically, we introduce another IDA up-sampler, sharing the same structure with the backbone decoder but having independent parameters, as our segmentation head. Its output channels are set to 1 to obtain a debris mask $\hat{M} \in \mathcal{R}^{W \times H \times 1}$ based on encoder features. The output mask is multiplied by F_b as follows:

$$F_{en} = \hat{M} \odot F_b \quad (7)$$

to acquire the enhanced feature $F_{en} \in \mathcal{R}^{W \times H \times C}$. F_{en} highlights debris features and removes background noise.

To ensure that the obtained mask \hat{S} accurately indicates the desired debris region, we use a Segmentation Loss to train the segmentation head. The mask S is supervised by a target mask S with the following loss function:

$$\mathcal{L}_{seg} = -\frac{1}{WH} \sum_{i=1, j=1}^{W, H} \left[M_{ij} \log(\hat{M}_{ij}) + (1 - M_{ij}) \log(1 - \hat{M}_{ij}) \right], \quad (8)$$

where W, H are image dimensions, M_{ij} is the ground truth, and \hat{M}_{ij} is the predicted probability. The obtained F_{en} is then passed through two modules: a Debris Detection module and a Debris Offset module.

4.4 Debris Detection Module

In each frame, we detect each line source by detecting its two endpoints. Two endpoints of each line source must be one on the left and one on the right. So, we design our model to produce a left-endpoint heatmap and a right-endpoint heatmap. The left-endpoint heatmap indicates left endpoints of all line sources, where the right one reflects right points. And then, we establish an endpoint embedding module to match different left and right endpoints belonging to a same line source together.

4.4.1 Endpoints Heatmap

The endpoints heatmap head is a convolutional layer that takes F_{en} as input and feedback heatmaps $\hat{H} \in \mathcal{R}^{W \times H \times 2}$, which has two channels that one for the left and one for the right endpoint. Each pixel in the heatmap represents the likelihood of the position being a line source endpoint.

Follow existing detection heatmap training pipeline, we utilize the focal loss to train the heatmap head as follows:

$$\mathcal{L}_{\text{hm}} = \frac{1}{N_{\text{pos}}} \sum_{whc} \text{Focal}(H, \hat{H}), \quad (9)$$

where \hat{H} and H are the predicted and the ground-truth heatmaps. w, h, c means the spatial and channel index. The ground-truth heatmaps H are generated by drawing Gaussian kernels at the positions of each endpoint.

4.4.2 Line Source Embedding

The line source embedding predicts features for each endpoint. Specifically, we predict a left endpoint line source embedding maps $\hat{E}_l \in \mathcal{R}^{W \times H \times C_2}$ and a right endpoint line source embedding maps $\hat{E}_r \in \mathcal{R}^{W \times H \times C_2}$. During inference, with the predicted endpoints heatmaps, we first derive local-maximum points for each heatmap, resulting in N left endpoints and M right endpoints. Then we utilize these points to take corresponding embeddings from \hat{E}_l and \hat{E}_r , respectively, denoted as $\{e_l^1, e_l^2, \dots, e_l^N\}$ and $\{e_r^1, e_r^2, \dots, e_r^M\}$. Based on these, we would compute an embedding similarity matrix $S^{\text{emb}} \in \mathcal{R}^{N \times M}$ where $S_{i,j}^{\text{emb}}$ is computed as follows:

$$S_{i,j}^{\text{emb}} = |(e_l^i - e_r^j)|. \quad (10)$$

$S_{i,j}^{\text{emb}}$ reflects similarity of i -th left point and j -th right point. With this, we provide a simple yet effective scheme, that each left point matches with its nearest neighbors right point to organize an endpoint pair as a detected object.

Inspired by CornerNet [33], we design the loss function of our embedding as follows:

$$\mathcal{L}_{\text{same}} = \frac{1}{K} \sum_{k=1}^K [(e_l^k - e_c^k)^2 + (e_r^k - e_c^k)^2], \quad (11)$$

where e_l^k and e_r^k are endpoint features, e_c^k is the mean of e_l^k and e_r^k , utilized to push e_l^k and e_r^k as close as possible. Meanwhile, we introduce $\mathcal{L}_{\text{diff}}$ to separate the features of different pairs as:

$$\mathcal{L}_{\text{diff}} = \frac{1}{K(K-1)} \sum_{k=1}^K \sum_{\substack{j=1 \\ j \neq k}}^K \max(0, \Delta - |e^k - e^j|), \quad (12)$$

where Δ is the minimum feature distance threshold. In our experiments, we set Δ to 1. This term facilitates to push center features belonging to different objects far away.

4.5 Debris Offset Module

We construct a Debris Offset module. For the t -th frame, this module predicts two offset maps, $\hat{O}_l^t \in \mathcal{R}^{W \times H \times 2}$ and $\hat{O}_r^t \in \mathcal{R}^{W \times H \times 2}$ for left and right endpoints, respectively.

During inference, the offset plays a key role in data association. Assume that the detection head provides N detected objects, we could index N offsets as: $\{(o_l^t)_1, (o_l^t)_2, \dots, (o_l^t)_N\}$ and $\{(o_r^t)_1, (o_r^t)_2, \dots, (o_r^t)_N\}$. They indicate object endpoint offsets between the current frame and the previous $t-1$ frame. With these predicted offsets, for each detected object, we could derive endpoint locations at the previous frame as follows:

$$\text{left: } (c')_l^{t-1} = c_l^t - o_l^t, \text{ right: } (c')_r^{t-1} = c_r^t - o_r^t, \quad (13)$$

where c' is the derived endpoint coordinate and c is the detected one. These derived endpoints imply the potential previous object locations. With these, we could match objects across frames by measuring the location consistency between the derived endpoints and the detected object endpoints. If the previous frame has M detected objects, we would compute a similarity matrix $S^{\text{obj}} \in \mathcal{R}^{N \times M}$ where $S_{i,j}^{\text{obj}}$ is computed as follows:

$$S_{i,j}^{\text{obj}} = |(c')_l^{t-1} - (c)_l^{t-1}| + |(c')_r^{t-1} - (c)_r^{t-1}|. \quad (14)$$

$S_{i,j}^{\text{obj}}$ reflects similarity of i -th object in the t -th frame and j -th object in the $t-1$ frame. Similar to the embedding module, we also utilize nearest neighbor as a matching scheme that the object in the current frame associates with its nearest neighbors in the previous frame.

To achieve the aforementioned function, during the training phase, we minimize the difference between the ground-truth offset and the predicted offset as follows:

$$\mathcal{L}_{\text{off}} = \frac{1}{K} \sum_{i=1}^K |(o^t)_i - [(c^t)_i - (c^{t-1})_i]|, \quad (15)$$

4.6 Loss function

Finally, the loss function \mathcal{L} is defined by the weighted summation of all loss terms,

$$\mathcal{L} = \lambda_{\text{seg}}\mathcal{L}_{\text{seg}} + \lambda_{\text{hm}}\mathcal{L}_{\text{hm}} + \lambda_{\text{emb}}(\mathcal{L}_{\text{same}} + \mathcal{L}_{\text{diff}}) + \lambda_{\text{off}}\mathcal{L}_{\text{off}}, \quad (16)$$

where λ_{seg} , λ_{hm} , λ_{emb} and λ_{off} represent the weights for \mathcal{L}_{seg} , \mathcal{L}_{hm} , $(\mathcal{L}_{\text{same}} + \mathcal{L}_{\text{diff}})$ and \mathcal{L}_{off} .

5 Experiments

Table 2: Comparison of trackers on Debris Test and Dense Debris Test. The table compares the performance of various tracking algorithms in two distinct scenarios. The **best** and **second-best** figures are in color and n represents the number of debris.

Tracker	Debris($n \leq 2$)						Dense Debris($1 \leq n \leq 5$)					
	IDF1 \uparrow	MOTA \uparrow	IDS \downarrow	HOTA \uparrow	DetA \uparrow	AssA \uparrow	IDF1 \uparrow	MOTA \uparrow	IDS \downarrow	HOTA \uparrow	DetA \uparrow	AssA \uparrow
LSD [34]	11.4	9.8	/	/	/	/	/	/	/	/	/	/
Deepsort [17]	71.7	55.3	211	56.4	56.9	55.8	72.9	57.8	1947	58.7	60.1	57.4
Moidt [35]	69.1	54.0	239	54.2	55.6	52.8	68.6	53.5	2015	53.9	55.7	52.2
CTracker [36]	83.4	71.0	240	72.9	74.3	71.5	69.3	61.7	1660	58.2	63.9	53.0
Sort+YoloX[37]	85.6	74.7	130	75.1	75.3	74.8	76.0	59.3	1394	61.5	61.7	61.3
Centertrack [21]	86.3	77.1	174	81.0	85.6	75.9	72.5	64.8	1292	66.1	76.7	56.9
ByteTrack [23]	91.0	83.3	195	82.8	83.9	81.6	79.4	62.8	1211	66.3	66.8	65.8
OCSORT [38]	91.6	84.1	138	83.7	84.9	82.5	82.6	68.5	1260	70.8	73.3	68.3
SDTNet (Ours)	91.8	87.7	169	87.8	90.9	84.8	80.6	70.3	1070	73.6	81.6	65.6

5.1 Experimental Setup

All experiments are performed using the mmdetection framework [39] with Pytorch [40]. The SDT-Net model is trained on 8 NVIDIA 4090 GPUs. The entire model is trained for 60 epochs, and the initial learning rate is set to $3e-3$, which is decayed by 0.1 at the 20 epoch. The association radius r to 200. Additionally, We adopt a downsampling strategy to generate paired images for training. Specifically, we first crop image patches of size 1524×1524 from the original high-resolution images as ground truth. We employ the resolution of the input images is set to 1524×1524 and the batch size is set to 2. Besides, the value of λ_{seg} and λ_{emb} are set to 1.0, λ_{hm} is set to 10, and λ_{off} is set to 0.1,

5.2 Evaluation Metrics

For evaluating the performance, we use standard MOT [41] evaluation metrics. Specifically, we adopt commonly used metrics in the field, including Multi-Object Tracking Accuracy (MOTA), identity F1 score (IDF1), Identity Switches (IDs), and Higher Order Tracking Accuracy (HOTA) [42]. These metrics provide a comprehensive assessment of tracking performance. Notably, HOTA includes Detection Accuracy (DetA) and Association Accuracy (AssA), where DetA measures the accuracy of detecting objects regardless of their identities, and AssA evaluates how well identities are consistently maintained across frames.

5.3 Comparison with Existing MOT Methods

As shown in Tab. 2, we compare our proposed SDT-Net with state-of-the-art MOT methods on the SDTD test set. Our method outperforms previous approaches in tracking space debris, particularly under dense debris conditions. Especially, SDT-Net significantly outperforms CenterTrack in tracking performance. On the debris test set, it improves MOTA and HOTA by 10.6% and 6.8%, respectively, while on the dense debris test set, the improvements are 5.5% and 7.5%. These results demonstrate that SDT-Net achieves superior object association (higher AssA) and detection robustness (higher DetA). As shown in Tab. 2, SDT-Net consistently outperforms CenterTrack across all key metrics, highlighting its effectiveness in complex space debris tracking scenarios.

5.4 Ablation Study

To analyze the contributions of different components in SDT-Net, we conduct an ablation study on the Debris Test and Dense Debris Test sets, as shown in Tab 3. We evaluate three configurations: (a) Based on Centertrack, the center point and box size parameters are used to predict line source debris, and the debris offset module is also included; (b) LSE

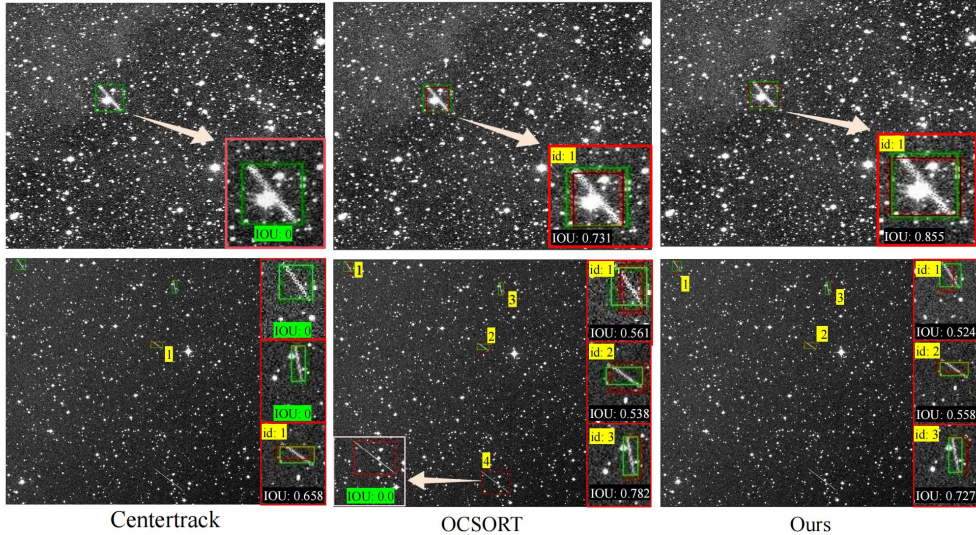


Figure 5: Visualization example of the tracking results of the SDTD model on the test set. The green bounding box represents the GT, and the red bounding box represents the model prediction result. When the Intersection over Union (IoU) between the predicted box and GT is 0, the presence of only a green box indicates a False Negative, while the presence of only a red box indicates a False Positive.

(Line Source Embedding), which models debris as line sources and directly locates their endpoint pairs; (c) RoI-FE (Region of Interest Feature Enhancement) further enhances the fragment feature representation and removes the debris offset module; and (d) Complete SDT-Net.

Effect of Line Source Embedding (LSE): Compared to CenterTrack (row a), introducing the line source embedding in SDT-Net (row b) leads to notable improvements across all metrics. Specifically, MOTA improves from 77.1% to 85.5% on the Debris Test set and from 64.8% to 64.9% on the Dense Debris Test set. This indicates that directly modeling debris as segments rather than center-based boxes provides better spatial localization, leading to improved object association (higher IDF1) and overall tracking performance.

Region-of-Interest Feature Enhancement (RoI-FE): Further incorporating segmentation masks (compare rows b and d) enhances the representation of debris features. This results in additional performance gains, with MOTA improving from 85.5% to 87.7% on the Debris Test set and from 64.9% to 70.3% on the Dense Debris Test set. Similarly, HOTA sees a significant increase, confirming that segmentation helps improve tracking robustness.

Offset Module: As shown in rows (c) and (d), introducing the debris offset module alone can significantly improve all indicators. Specifically, MOTA is improved from 86.0% (row c) to 87.7% on the fragmented test set, and from 62.9% to 70.3% on the dense fragmented test set. These improvements show that the offset module plays a key role in improving endpoint accuracy and overall tracking robustness. Finally, after integrating all modules, IDF1 is 80.6%, MOTA is 70.3%, and HOTA is 73.6% on the dense fragmented test set.

Table 3: Ablation study of SDT-Net.

	LSE	RoI-FE	Offset Module	Debris Test ($n \leq 2$)				Dense Debris Test ($1 \leq n \leq 5$)			
				IDF1↑	MOTA↑	HOTA↑	DetA↑	IDF1↑	MOTA↑	HOTA↑	DetA↑
(a)			✓	86.3	77.1	81.0	85.6	72.5	64.8	66.1	76.7
(b)	✓		✓	90.4	85.5	84.8	88.3	78.5	64.9	65.3	79.1
(c)	✓	✓		88.2	86.0	85.2	88.9	73.5	62.9	63.0	78.6
(d)	✓	✓	✓	91.8	87.7	87.8	90.9	80.6	70.3	73.6	81.6

The complete SDT-Net (row c) achieves the best performance, demonstrating that combining LSE and RoI-FE leads to the most accurate debris tracking. These results highlight that directly predicting line source endpoints improves accuracy, while segmentation masks further strengthen debris features, particularly in challenging dense debris scenarios.

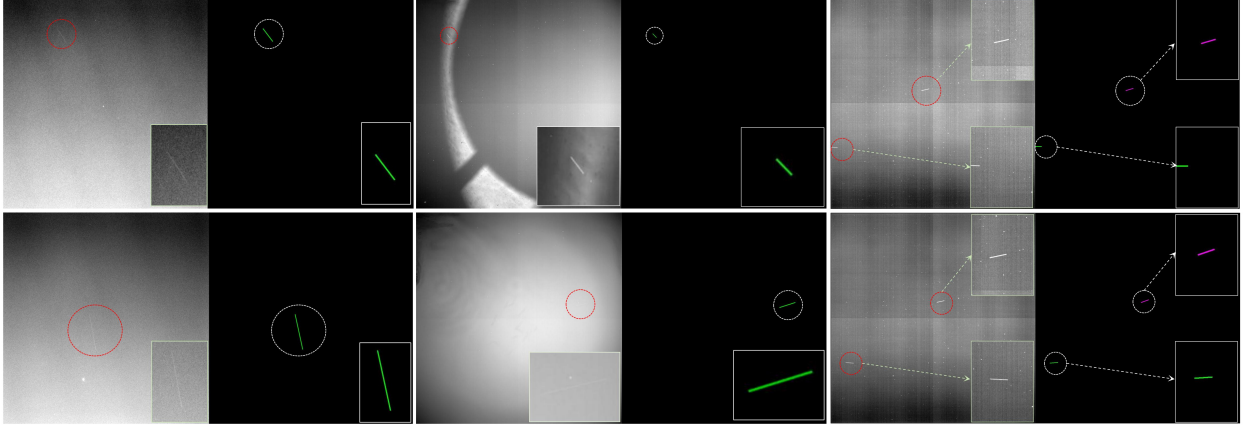


Figure 6: Visualization of sample tracking results of real-world observations. Left: real-world debris observation. Right: model predicts tracking results, represented by predicted endpoints and connecting segments forming the trajectory (superimposed on a blank background). Different colors correspond to different debris IDs.

5.5 Qualitative Results

We compare it with state-of-the-art tracking methods, including OCSORT and CenterTrack, in complex scenarios. Fig. 5 illustrates the tracking results on datasets containing space debris with cluttered backgrounds, occlusions, and varying object densities.

CenterTrack fails to maintain debris tracking when occluded by light sources, whereas SDTD successfully detects and tracks the debris in such situations. In scenarios with dense debris, OCSORT produces false positives, while SDTD exhibits superior spatial detection and tracking capabilities. This reflects its ability to accurately associate and locate dense debris.

To further verify the effectiveness of SDT-Net, we evaluate the model with real-world debris data. Due to the scarcity of real-world debris observation data, we finally select 36 video sequences containing debris (a total of 2,228 frames) and invited astronomy experts to annotate the real-world observation data. As shown in Table 4, our method (SDT-Net) achieves a MOTA score exceeding 73%, demonstrating strong real-world performance. Fig 6 further illustrates the effectiveness of our approach. The left side of the figure presents raw debris observations, while the right side visualizes the predicted tracking results. Notably, the right side does not represent ground truth but rather our model’s predictions. For clarity, we display each tracked object using a line connecting its two key points instead of conventional bounding boxes. In practical applications, these tracked trajectories are overlaid on blank background images to facilitate interpretation. Each color in the visualization corresponds to a distinct debris ID, reflecting the model’s ability to distinguish and track multiple objects.

Table 4: Evaluation of SDT-Net on the Antarctic Station real-world data.

Method	MOTA \uparrow	HOTA \uparrow	DetA \uparrow
Deepsort [17]	48.7	48.9	51.8
Motdt [35]	47.4	45.2	47.6
CTracker [36]	51.9	45.8	54.5
Sort+YoloX [37]	57.4	57.4	58.9
CenterTrack [21]	64.7	58.3	68.7
ByteTrack [23]	66.8	62.4	70.1
OCSORT [38]	69.3	66.8	72.2
SDT-Net	73.2	68.1	75.8

6 Conclusion

In this paper, we introduce SDTD, the first benchmark dataset for space debris tracking. SDTD consisting of 18,040 videos from ZTF with 62,562 frames and 250,000 synthetic debris. SDTD provides diverse scenarios, including complex backgrounds and dense debris. Based on this, we propose a deep learning-based tracking network, SDTD, which achieves state-of-the-art performance. Furthermore, we conduct a user study on real-world data to assess the model’s generalization ability. The results demonstrate that SDT-Net not only performs well on real debris scenes (e.g., Antarctic Station data) but also exhibits transferability to out-of-distribution scenarios, ensuring robust tracking capabilities in challenging environments.

References

- [1] JI Katz. Can a satellite dodge space debris? *Acta Astronautica*, 2024.
- [2] Michael A Steindorfer, Peiyuan Wang, Franz Koidl, and Georg Kirchner. Space debris and satellite laser ranging combined using a megahertz system. *Nature Communications*, 16(1):1–12, 2025.
- [3] Ruiming Liu, Yanhong Lu, Chenglong Gong, and Yang Liu. Infrared point target detection with improved template matching. *Infrared Physics & Technology*, 55(4):380–387, 2012.
- [4] Timothy S Murphy, Marcus J Holzinger, and Brien Flewelling. Space object detection in images using matched filter bank and bayesian update. *Journal of Guidance, Control, and Dynamics*, 40(3):497–509, 2017.
- [5] Min-Song Wei, Fei Xing, and Zheng You. A real-time detection and positioning method for small and weak targets using a 1d morphology-based approach in 2d images. *Light: Science & Applications*, 7(5):18006–18006, 2018.
- [6] Ping Jiang, Chengzhi Liu, Wenbo Yang, Zhe Kang, and Zhenwei Li. Automatic space debris extraction channel based on large field of view photoelectric detection system. *Publications of the Astronomical Society of the Pacific*, 134(1032):024503, 2022.
- [7] Zhengxia Zou, Keyan Chen, Zhenwei Shi, Yuhong Guo, and Jieping Ye. Object detection in 20 years: A survey. *Proceedings of the IEEE*, 111(3):257–276, 2023.
- [8] Sajid Javed, Martin Danelljan, Fahad Shahbaz Khan, Muhammad Haris Khan, Michael Felsberg, and Jiri Matas. Visual object tracking with discriminative filters and siamese networks: a survey and outlook. *IEEE transactions on pattern analysis and machine intelligence*, 45(5):6552–6574, 2022.
- [9] Hui Li, Bo Chen, Li Feng, Ying Li, Yu Huang, Jing-Wei Li, Lei Lu, Jian-Chao Xue, Bei-Li Ying, Jie Zhao, et al. The lyman-alpha solar telescope (1st) for the aso-s mission—i. scientific objectives and overview. *Research in Astronomy and Astrophysics*, 19(11):158, 2019.
- [10] Tinggui Wang, Guilin Liu, Zhenyi Cai, Jinjun Geng, Min Fang, Haoning He, Ji-an Jiang, Ning Jiang, Xu Kong, Bin Li, et al. Science with the 2.5-meter wide field survey telescope (wfst). *Science China Physics, Mechanics & Astronomy*, 66(10):109512, 2023.
- [11] Bin Lin, Lijun Zhong, Sheng Zhuge, Xia Yang, Yang Yang, Kunpeng Wang, and Xiaohu Zhang. A new pattern for detection of streak-like space target from single optical images. *IEEE Transactions on Geoscience and Remote Sensing*, 60:1–13, 2021.
- [12] JR Peterson, JG Jernigan, SM Kahn, AP Rasmussen, E Peng, Z Ahmad, J Bankert, C Chang, C Claver, DK Gilmore, et al. Simulation of astronomical images from optical survey telescopes using a comprehensive photon monte carlo approach. *The Astrophysical Journal Supplement Series*, 218(1):14, 2015.
- [13] Marshall D Perrin, Anand Sivaramakrishnan, Charles-Philippe Lajoie, Erin Elliott, Laurent Pueyo, Swara Ravindranath, and Loïc Albert. Updated point spread function simulations for jwst with webbpf. In *Space telescopes and instrumentation 2014: optical, infrared, and millimeter wave*, volume 9143, pages 1174–1184. SPIE, 2014.
- [14] Jiang Tao, Yunfeng Cao, and Meng Ding. Sdebrisnet: A spatial–temporal saliency network for space debris detection. *Applied Sciences*, 13(8):4955, 2023.
- [15] Zijian Zhu, Ali Zia, Xuesong Li, Bingbing Dan, Yuebo Ma, Enhai Liu, and Rujin Zhao. Sstd: Stripe-like space target detection using single-point weak supervision. *arXiv preprint arXiv:2407.18097*, 2024.
- [16] Andreas Geiger, Philip Lenz, and Raquel Urtasun. Are we ready for autonomous driving? the kitti vision benchmark suite. In *2012 IEEE conference on computer vision and pattern recognition*, pages 3354–3361. IEEE, 2012.

- [17] Alex Bewley, Zongyuan Ge, Lionel Ott, Fabio Ramos, and Ben Upcroft. Simple online and realtime tracking. In *2016 IEEE international conference on image processing (ICIP)*, pages 3464–3468. Ieee, 2016.
- [18] Greg Welch, Gary Bishop, et al. An introduction to the kalman filter. 1995.
- [19] Harold W Kuhn. The hungarian method for the assignment problem. *Naval research logistics quarterly*, 2(1-2):83–97, 1955.
- [20] Nicolai Wojke, Alex Bewley, and Dietrich Paulus. Simple online and realtime tracking with a deep association metric. In *2017 IEEE international conference on image processing (ICIP)*, pages 3645–3649. IEEE, 2017.
- [21] Xingyi Zhou, Vladlen Koltun, and Philipp Krähenbühl. Tracking objects as points. In *European conference on computer vision*, pages 474–490. Springer, 2020.
- [22] Xingyi Zhou, Dequan Wang, and Philipp Krähenbühl. Objects as points. *arXiv preprint arXiv:1904.07850*, 2019.
- [23] Yifu Zhang, Peize Sun, Yi Jiang, Dongdong Yu, Fucheng Weng, Zehuan Yuan, Ping Luo, Wenyu Liu, and Xinggang Wang. Bytetrack: Multi-object tracking by associating every detection box. In *European conference on computer vision*, pages 1–21. Springer, 2022.
- [24] Ping Jiang, Chengzhi Liu, Wenbo Yang, Zhe Kang, Cunbo Fan, and Zhenwei Li. Space debris automation detection and extraction based on a wide-field surveillance system. *The Astrophysical Journal Supplement Series*, 259(1):4, 2022.
- [25] Yang Guo, Xianlong Yin, Yao Xiao, Zhengxu Zhao, Xu Yang, and Chenggang Dai. Enhanced yolov8-based method for space debris detection using cross-scale feature fusion. *Discover Applied Sciences*, 7(2):95, 2025.
- [26] Peng Jia, Qiang Liu, and Yongyang Sun. Detection and classification of astronomical targets with deep neural networks in wide-field small aperture telescopes. *The Astronomical Journal*, 159(5):212, 2020.
- [27] Shaoqing Ren, Kaiming He, Ross Girshick, and Jian Sun. Faster r-cnn: Towards real-time object detection with region proposal networks. *Advances in neural information processing systems*, 28, 2015.
- [28] Kaiming He, Xiangyu Zhang, Shaoqing Ren, and Jian Sun. Deep residual learning for image recognition. In *Proceedings of the IEEE conference on computer vision and pattern recognition*, pages 770–778, 2016.
- [29] Eric Bellm. The zwicky transient facility. In *The Third Hot-wiring the Transient Universe Workshop*, volume 27, 2014.
- [30] Harry Edward Payne, Robert I Jedrzejewski, and Richard N Hook. Astronomical data analysis software and systems xii. *Astronomical Data Analysis Software and Systems XII*, 295, 2003.
- [31] Vladimir Koupryanov. Distinguishing features of ccd astrometry of faint geo objects. *Advances in Space Research*, 41(7):1029–1038, 2008.
- [32] Fisher Yu, Dequan Wang, Evan Shelhamer, and Trevor Darrell. Deep layer aggregation. In *Proceedings of the IEEE conference on computer vision and pattern recognition*, pages 2403–2412, 2018.
- [33] Hei Law and Jia Deng. Cornernet: Detecting objects as paired keypoints. In *Proceedings of the European conference on computer vision (ECCV)*, pages 734–750, 2018.
- [34] Rafael Grompone Von Gioi, Jérémie Jakubowicz, Jean-Michel Morel, and Gregory Randall. Lsd: A line segment detector. *Image Processing On Line*, 2:35–55, 2012.
- [35] Long Chen, Haizhou Ai, Zijie Zhuang, and Chong Shang. Real-time multiple people tracking with deeply learned candidate selection and person re-identification. In *2018 IEEE international conference on multimedia and expo (ICME)*, pages 1–6. IEEE, 2018.
- [36] Jinlong Peng, Changan Wang, Fangbin Wan, Yang Wu, Yabiao Wang, Ying Tai, Chengjie Wang, Jilin Li, Feiyue Huang, and Yanwei Fu. Chained-tracker: Chaining paired attentive regression results for end-to-end joint multiple-object detection and tracking. In *Computer Vision—ECCV 2020: 16th European Conference, Glasgow, UK, August 23–28, 2020, Proceedings, Part IV 16*, pages 145–161. Springer, 2020.
- [37] Z Ge. Yolox: Exceeding yolo series in 2021. *arXiv preprint arXiv:2107.08430*, 2021.
- [38] Jinkun Cao, Jiangmiao Pang, Xinshuo Weng, Rawal Khirodkar, and Kris Kitani. Observation-centric sort: Rethinking sort for robust multi-object tracking. In *Proceedings of the IEEE/CVF conference on computer vision and pattern recognition*, pages 9686–9696, 2023.
- [39] Kai Chen, Jiaqi Wang, Jiangmiao Pang, Yuhang Cao, Yu Xiong, Xiaoxiao Li, Shuyang Sun, Wansen Feng, Ziwei Liu, Jiarui Xu, et al. Mmdetection: Open mmlab detection toolbox and benchmark. *arXiv preprint arXiv:1906.07155*, 2019.

- [40] Adam Paszke, Sam Gross, Francisco Massa, Adam Lerer, James Bradbury, Gregory Chanan, Trevor Killeen, Zeming Lin, Natalia Gimelshein, Luca Antiga, et al. Pytorch: An imperative style, high-performance deep learning library. *Advances in neural information processing systems*, 32, 2019.
- [41] Keni Bernardin and Rainer Stiefelhagen. Evaluating multiple object tracking performance: the clear mot metrics. *EURASIP Journal on Image and Video Processing*, 2008:1–10, 2008.
- [42] Jonathon Luiten, Aljosa Osep, Patrick Dendorfer, Philip Torr, Andreas Geiger, Laura Leal-Taixé, and Bastian Leibe. Hota: A higher order metric for evaluating multi-object tracking. *International journal of computer vision*, 129:548–578, 2021.

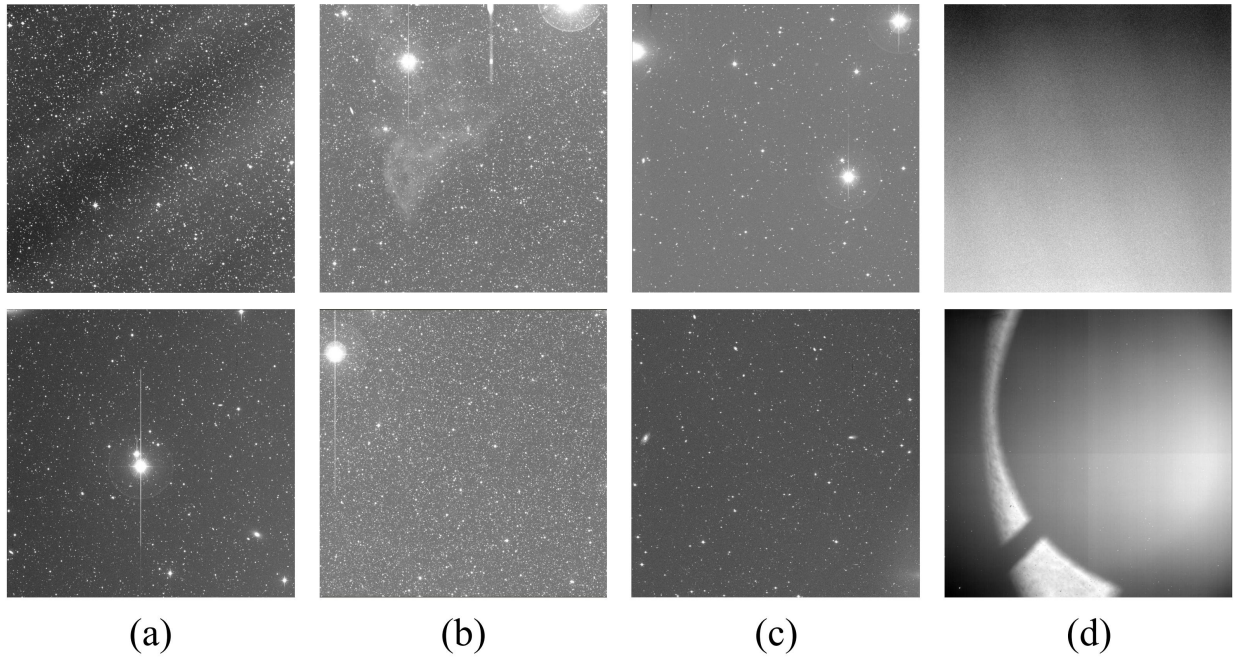


Figure 7: Data example of complex skylight background.

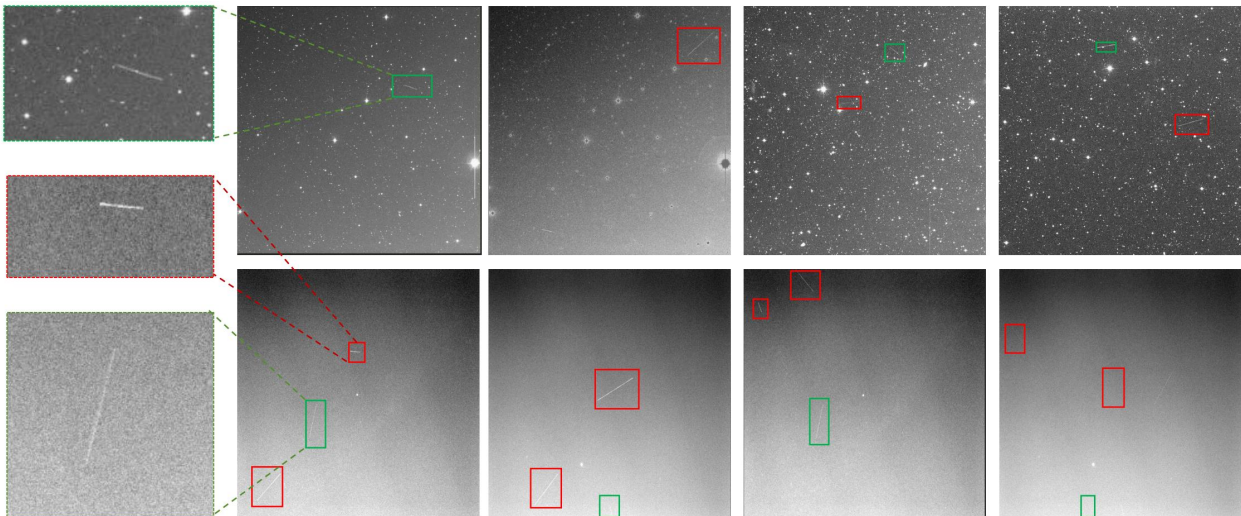


Figure 8: Comparison of debris simulation and real-world debris. The green bounding box represents real-world debris, and the red bounding box represents simulated debris.

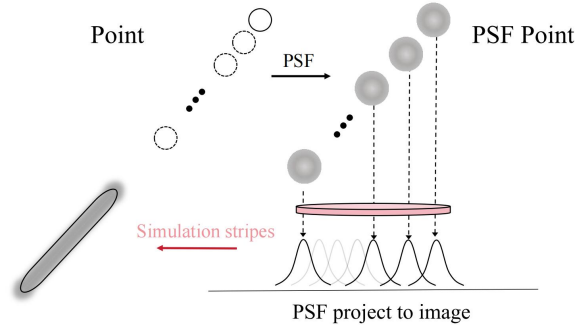


Figure 9: Dynamic imaging process of space debris.

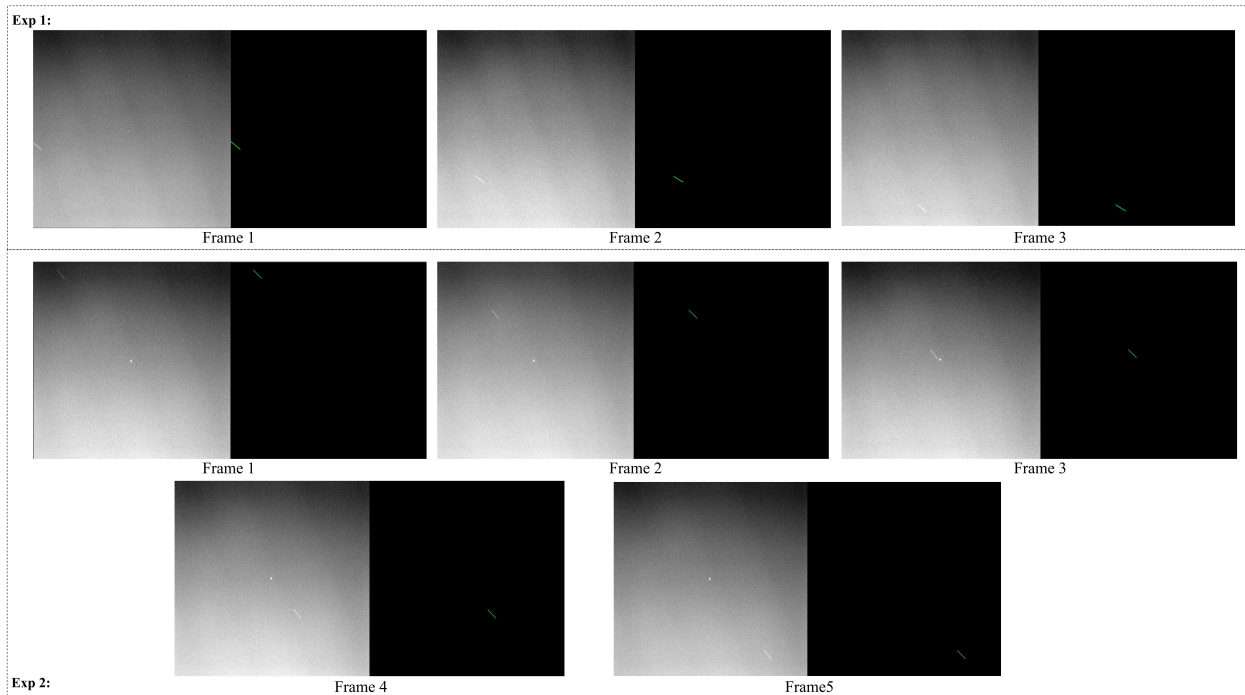


Figure 10: SDT-Net tracking results in the real-world data.

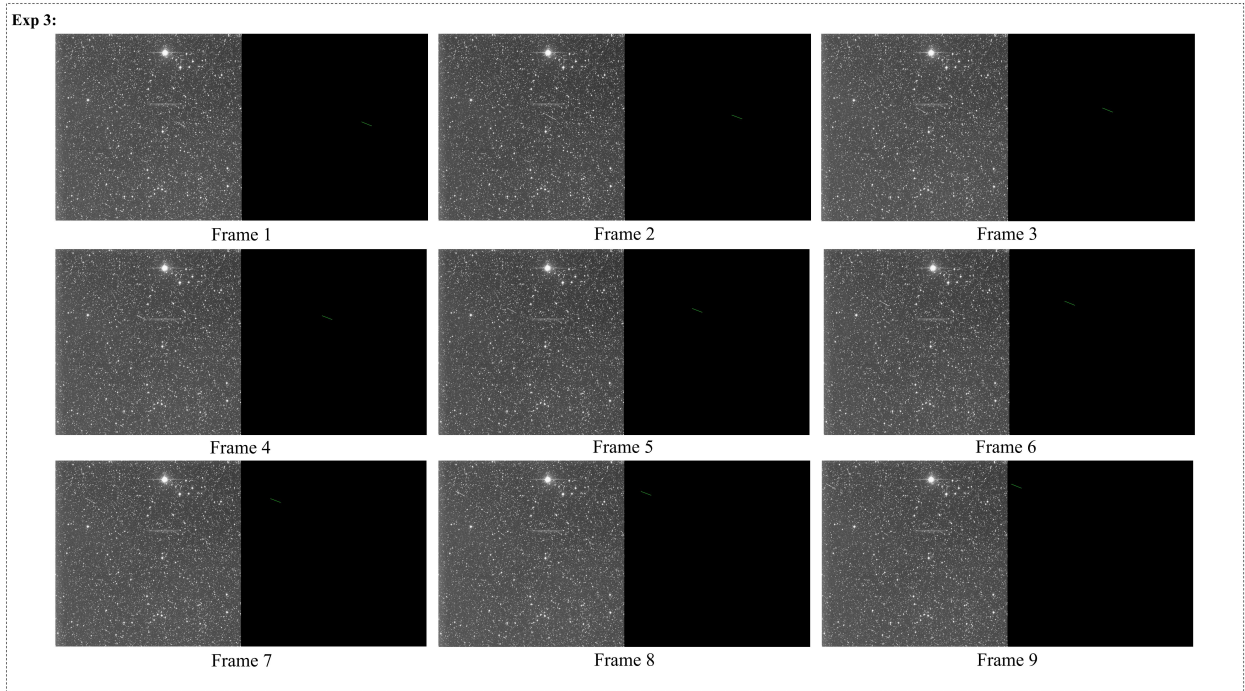


Figure 11: SDT-Net test tracking result example in SDTD.

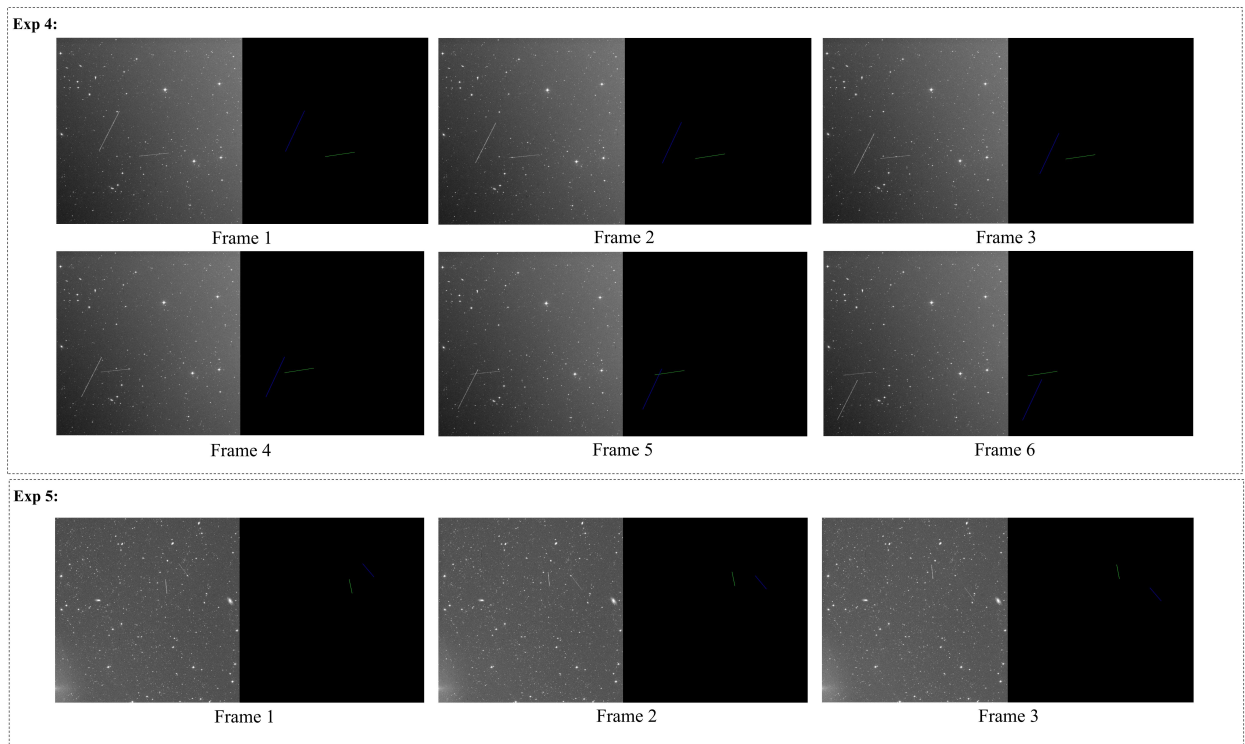


Figure 12: SDT-Net test tracking result example in SDTD, including at least two debris.